In vivo imaging of nanoparticle-labeled CAR T cells

Louise Kiru[a], Aimen Zlitni[a], Aidan Michael Tousley[b], Guillermo Nicolás Dalton[b], Wei Wu[a], Famyrah Lafortune[a], Anna Liu[c], Kristen May Cunanan[a], Hossein Nejadnik[d], Todd Sulchek[c], Michael Eugene Moseley[a], Robbie G. Majzner[b,e], and Heike Elisabeth Daldrup-Link[a,b,e,1]

[a]Department of Radiology, Molecular Imaging Program at Stanford, Stanford University, Stanford, CA 94305; [b]Department of Pediatrics, Stanford University, Stanford, CA 94305; [c]Department of Biomedical Engineering, Georgia Institute of Technology, Atlanta, GA 30332; [d]Department of Radiology, Hospital of the University of Pennsylvania, Philadelphia, PA 19104; and [e]Stanford Cancer Institute, Stanford University, Stanford, CA 94305

Edited by Catherine Murphy, Department of Chemistry, University of Illinois at Urbana–Champaign, Urbana, IL; received February 8, 2021; accepted December 10, 2021

Metastatic osteosarcoma has a poor prognosis with a 2-y, event-free survival rate of ∼15 to 20%, highlighting the need for the advancement of efficacious therapeutics. Chimeric antigen receptor (CAR) T-cell therapy is a potent strategy for eliminating tumors by harnessing the immune system. However, clinical trials with CAR T cells in solid tumors have encountered significant challenges and have not yet demonstrated convincing evidence of efficacy for a large number of patients. A major bottleneck for the success of CAR T-cell therapy is our inability to monitor the accumulation of the CAR T cells in the tumor with clinical-imaging techniques. To address this, we developed a clinically translatable approach for labeling CAR T cells with iron oxide nanoparticles, which enabled the noninvasive detection of the iron-labeled T cells with magnetic resonance imaging (MRI), photoacoustic imaging (PAT), and magnetic particle imaging (MPI). Using a custom-made microfluidics device for T-cell labeling by mechanoporation, we achieved significant nanoparticle uptake in the CAR T cells, while preserving T-cell proliferation, viability, and function. Multimodal MRI, PAT, and MPI demonstrated homing of the T cells to osteosarcomas and off-target sites in animals administered with T cells labeled with the iron oxide nanoparticles, while T cells were not visualized in animals infused with unlabeled cells. This study details the successful labeling of CAR T cells with ferumoxytol, thereby paving the way for monitoring CAR T cells in solid tumors.

ferumoxytol | CAR T cells | mechanoporation | multimodal imaging | magnetic resonance imaging

Clinical advances in the treatment of osteosarcoma have reached a plateau, and the survival rate has remained stagnant for over two decades (1). The prognosis for children with refractory, relapsed, and metastasized osteosarcoma remains poor with typically a 2-y event-free survival rate of 15 to 20% (2). Therefore, new therapeutics are urgently needed. Recent studies have shown promising results using chimeric antigen receptor (CAR) T cells that were targeted to the immune checkpoint molecule B7-H3 (CD276), a tumor antigen that is significantly up-regulated in osteosarcoma (3). The molecule is a member of the B7 and CD28 families and is broadly expressed on tumor cells, in which it is thought to play an inhibitory role on T-cell function (4).

CD19-targeted CAR T-cell therapies have demonstrated remarkable efficacy in the treatment of CD19-expressing tumors as well as in advanced, chemotherapy-resistant leukemia and lymphoma (5–7). However, responses in patients receiving T-cell therapy have been variable (8–10). A diagnostic technique that could noninvasively monitor the localization and expansion of the CAR T cells in tumors and off-target sites would help optimize personalized treatment regimens and combination therapies. Strategies used by clinical investigators to assess the activity of infused CAR T cells consist of flow cytometry, immunohistochemistry, and qPCR of peripheral blood samples or biopsies of sites of CAR T-cell activity including bone marrow, tumors, and lymph nodes (9, 10). While they provide suitable information, flow cytometry measurements of the expression of the CAR gene in circulating T cells represents the response in the periphery and not the tumor site (11), and repeated invasive biopsies are not practical in most clinical trials (12).

Magnetic resonance imaging (MRI) (13–15) and positron emission tomography (PET) (16–18) have been used to visualize therapeutic T cells in human subjects. Ahrens and coworkers used perfluorocarbon emulsion to label CAR T cells expressing antiepidermal growth factor receptor variant III (EGFRvIII), and they quantified the labeling of the T cells using fluorine-19 NMR after intravenous injection of the CAR T cells in mice bearing U87-EGFRvIII tumors (19). Additionally, imaging of EGFRvIII CAR T cells labeled with ultrasmall superparamagnetic iron oxide nanoparticles trafficking to human U-87 MG glioblastomas (20) and ferucarbotran-labeled, pmel-specific DsRed T cells accumulating in murine KR158B luciferase expressing glioblastomas (21) has also been reported. Furthermore, others have used enzymes (22), transporters (23), or membrane proteins (24) that facilitated the accumulation of radiotracers, for example, 9-(4-[^{18}F]fluoro-3-(hydroxymethyl) butyl)guanine in glioblastoma (17, 25). This requires genetic modification of the therapeutic cells, which, using previous viral packaging capacity, can result in immunogenicity and could potentially interfere with their function (26).

Significance

Chimeric antigen receptor (CAR) T-cell therapy is approved by the US Food and Drug Administration (FDA) for the treatment of B-cell acute lymphoblastic leukemia. Efforts are now underway to evaluate the efficacy of CAR T-cell therapy in solid tumors. However, a key limitation in the advancement of T-cell therapy is the lack of information on the biodistribution of the T cells in patients. Therefore, there is a need for the identification of translatable methods for tracking the therapeutic T cells noninvasively. We describe the mechanical labeling of CAR T cells with an FDA-approved iron oxide nanoparticle to demonstrate the noninvasive and multimodal imaging of the CAR T cells. This method may be utilized for monitoring T cells in clinical trials.

Author contributions: L.K., H.N., and H.E.D.-L. designed research; L.K., A.Z., A.M.T., G.N.D., and W.W. performed research; L.K., A.Z., A.M.T., F.L., and K.M.C. analyzed data; LK., A.Z., K.M.C., T.S., R.G.M., and M.E.M. contributed new reagents/analytic tools; and L.K. and H.E.D.-L. wrote the paper.

Competing interest statement: R.G.M. is a consultant for Lyell Immunopharma, Illumina Radiopharmaceuticals, and GammaDelta Therapeutics. T.S. is a cofounder of CellFE and a consultant for Heat Bio.

This article is a PNAS Direct Submission.

[1]To whom correspondence may be addressed. Email: heiked@stanford.edu.

This article contains supporting information online at http://www.pnas.org/lookup/suppl/doi:10.1073/pnas.2102363119/-/DCSupplemental.

Published January 31, 2022.

An ideal method for imaging intravenously infused CAR T cells should 1) utilize a widely available clinical-imaging technique, 2) use a translatable-imaging agent, 3) be nonimmunogenic, 4) provide low background in off-target tissues, and 5) provide quantitative measurements. To address these requirements, we developed a MRI-based cell-tracking technique, because MRI is already routinely used to monitor osteosarcomas in patients. We used the Food and Drug Administration (FDA)–approved iron supplement, ferumoxytol, "off label" as a cell marker, because ferumoxytol is composed of iron oxide nanoparticles that can be detected with MRI (27). Administration of ferumoxytol nanoparticles in children and young adults did not result in any signs of liver toxicity, hematologic, or kidney impairments (28); therefore, it is safe to use in humans. Ferumoxytol nanoparticles can also be detected with magnetic particle imaging (MPI), which provides high target to background contrast (29) and quantitative measurements (30).

Other therapeutic cells have been detected with ferumoxytol MRI in rodents (31–33), porcine animal models (34), and patients (28). However, no group has successfully labeled and tracked CAR T cells *in vivo* with ferumoxytol thus far. This is because transfection agents that are usually used to shuttle iron oxide nanoparticles into target cells, show low efficiency in T cells (35–37), and should be avoided for clinical applications (35). We used a custom-made microfluidics device (38) for mechanoporation-labeling of human anti-B7-H3 CAR T cells with ferumoxytol. This mechanical-labeling method does not require transfection agents or genetic manipulation of the cells.

The goal of our study was to develop a clinically translatable approach to label CAR T cells with nanoparticles for noninvasive cell-tracking using MRI, photoacoustic imaging (PAT), and MPI, while confirming cell viability with bioluminescence imaging (BLI). We demonstrated the detection of ferumoxytol-labeled CAR T cells localizing in osteosarcomas using MRI, PAT, and MPI, paving the way for clinical translation of this approach.

Results

Expression of the Anti-B7-H3 CAR in Human T Cells. A retroviral construct was engineered for the expression of the anti-B7-H3-4–1BBζ CAR (3) with the insertion of a BFP sequence downstream of the CD3ζ domain. Flow cytometry of the T cells transduced with the anti-B7-H3 gene indicated a transduction efficiency of 74.72 ± 3.23% compared to 0.94 ± 0.26% in the nontransduced (NT) T cells (Fig. 1*A*).

Mechanoporation Leads to Significant Uptake of Nanoparticles in CAR T Cells. The B7-H3 CAR T cells that were processed through a microfluidics device with ferumoxytol (10 mg/mL) demonstrated significantly higher uptake of iron per cell compared to the unlabeled cells (1.19 ± 0.03 pg/cell versus 0.02 ± 0.01 pg/cell, $P < 0.0001$), as determined by inductively coupled plasma-optical emission spectrometry (ICP-OES; Fig. 1*B*). This was further verified by 3,3'-diaminobenzidine (DAB)-Perl's Prussian blue staining (Fig. 1*C*). A comparison of the labeling efficiency using mechanoporation and passive coincubation of the B7-H3 CAR T cells with ferumoxytol indicated that the uptake of the iron oxide nanoparticles in the CAR T cells using the microfluidics device was significantly greater ($P < 0.0001$) compared to coincubation of the T cells with ferumoxytol (*SI Appendix*, Fig. 1).

Cell Viability Was Maintained in the T Cells That Were Labeled by Mechanoporation. The effect of mechanoporation on T-cell viability immediately post labeling was determined by the trypan blue exclusion method, and the effect of mechanoporation on T-cell proliferation was assessed with the Cell Counting Kit-8 (CCK-8) assay at Day 1, 3, and 5 post labeling. The percentage cell viability was not significantly different for the anti-B7-H3 CAR T cells before labeling compared to the anti-B7-H3 CAR T cells immediately after labeling (96.15 ± 0.63% versus 96.12 ± 0.35%, $P = 0.96$; Fig. 1*D*). Further analysis of the population doubling time (PDT) revealed that the doubling time for the iron-labeled T cells was 2.57 d compared to 3.46 d for the unlabeled T cells, indicating that the cells containing iron were proliferating 1.35-fold faster than the unlabeled cells (*SI Appendix*, Fig. 2). In addition, the CCK-8 assay showed that the proliferation of the unlabeled and labeled B7-H3 CAR T cells was not significantly different at D1 (0.110 ± 0.001 versus 0.110 ± 0.001, $P = 0.523$), D3 (0.139 ± 0.002 versus 0.139 ± 0.002, $P = 0.888$), and D5 (0.165 ± 0.002 versus 0.170 ± 0.002, $P = 0.402$) post labeling (Fig. 1*E*).

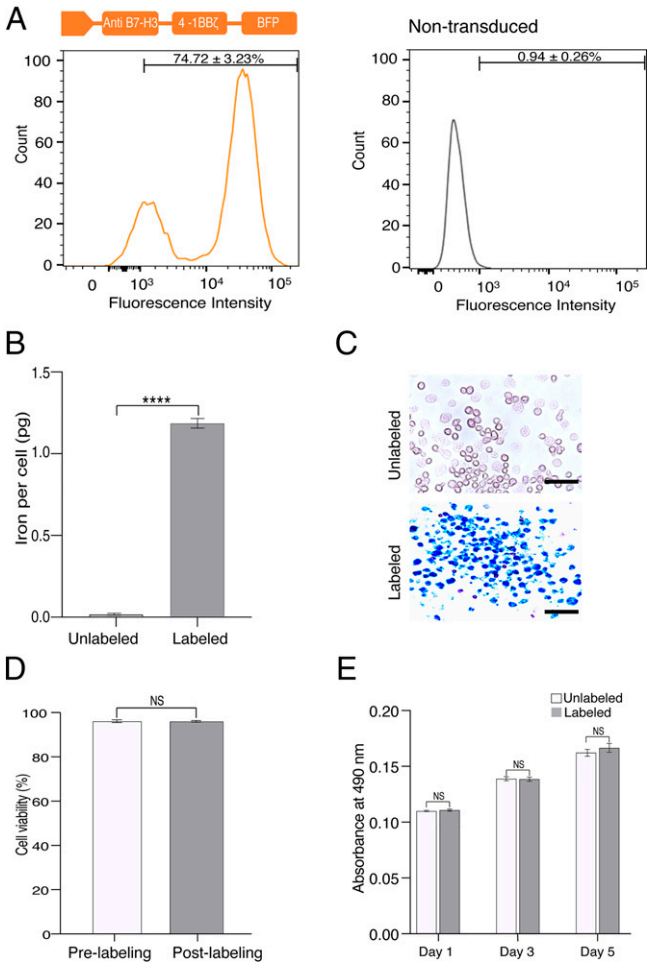

Fig. 1. The expression profile and labeling efficiency of B7-H3 CAR T cells. (*A*) Representative flow cytometry histograms obtained on Day 10 post transduction displaying the mean transduction efficiency of anti-B7-H3 CAR T cells (74.72 ± 3.23%) and NT T cells (0.94 ± 0.26%). (*B*) Measurements of the iron per cell levels using ICP-OES revealed significantly higher ($P < 0.0001$) uptake of ferumoxytol in the labeled T cells than unlabeled T cells. (*C*) Prussian blue staining showing greater accumulation of iron in the T cells labeled with ferumoxytol than the unlabeled T cells (Scale bar, 50 μm). (*D*) Trypan blue exclusion method showed no significant difference in the cell viability of the unlabeled or ferumoxytol-labeled anti-B7-H3 CAR T cells. (*E*) Proliferation of the unlabeled or ferumoxytol-labeled anti-B7-H3 CAR T cells was not significantly different on Day 1, 3, and 5, as determined by the CCK-8 assay. Data represents mean ± SEM, and n is ≥ 3 per group. Statistical comparisons were performed using an unpaired Student *t* test.

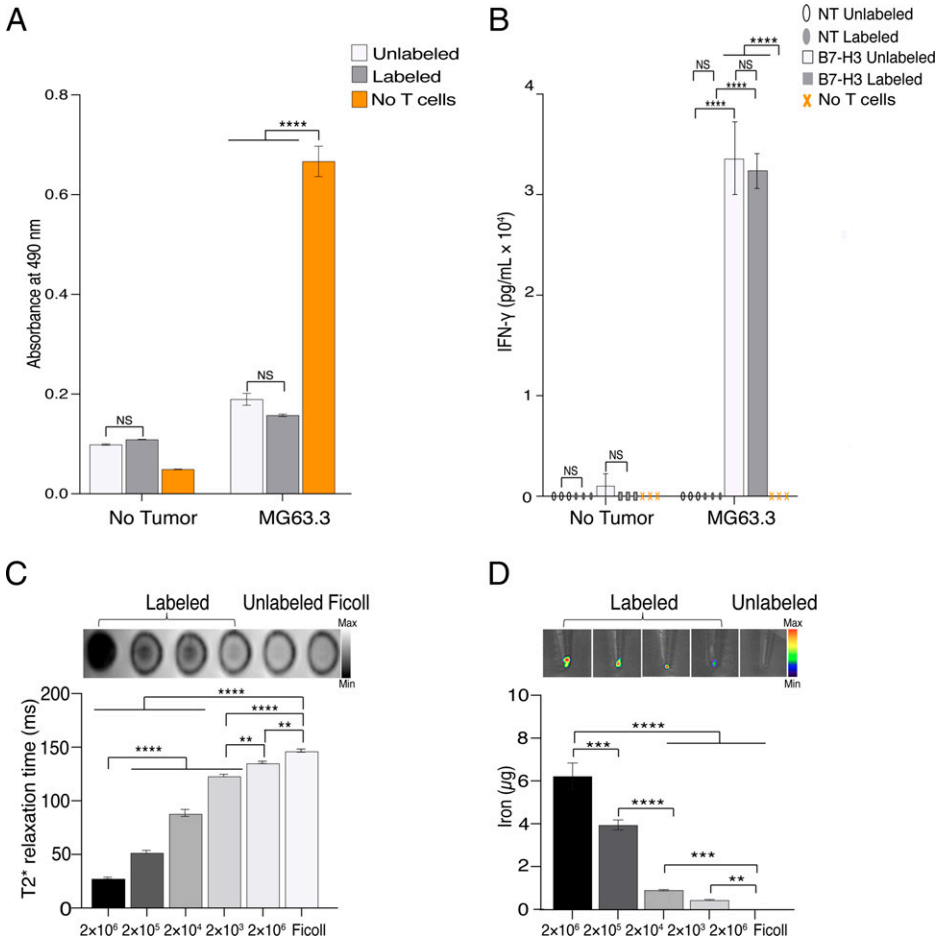

Fig. 2. Function of the CAR T cells was maintained *in vitro*. (*A*) The CCK-8 assay indicated that the proliferation of the T cells labeled with ferumoxytol and the unlabeled T cells was not significantly different ($P > 0.99$), while the coculture of the anti-B7-H3 CAR T cells with the target tumor cells at a 1:1 ratio revealed a 1.2-fold decrease in the viability of MG63.3 cells cocultured with the labeled anti-B7-H3 CAR T cells compared to the unlabeled cells. (*B*) Cytokine release was maintained following mechanoporation. The release of IFNγ in the T cells labeled with ferumoxytol and coincubated with or without tumor cells was not significantly different from the unlabeled cells. (*C*) Quantitative ROI analysis of T2* images demonstrated that the limit of detection for MRI was 2×10^4 pelleted T cells labeled with ferumoxytol, while (*D*) the limit of detection for MPI was 2×10^3 pelleted T cells. Data represents mean ± SEM, and n is ≥ 4 per group. Statistical comparisons were performed using the one-way ANOVA with the Tukey's honest significant difference test.

Labeling the CAR T cells with ferumoxytol does not affect T-cell function. The ferumoxytol-labeled anti-B7-H3 CAR T cells were subjected to *in vitro* functional assays to evaluate whether the mechanoporation process and ferumoxytol-labeling would affect the function of the anti-B7-H3 CAR T cells. Coincubation of B7-H3 CAR T cells and MG63.3 osteosarcoma cells indicated that mechanoporation did not alter the proliferation and function of the T cells. The absorbance at 490 nm was not significantly different for the unlabeled versus labeled T cells that were incubated alone (0.10 ± 0.001 versus 0.11 ± 0.001, $P > 0.99$). There was a 1.2-fold decrease in the viability of the MG63.3 cells cocultured with the labeled B7-H3 CAR T cells compared to MG63.3 cells cocultured with the unlabeled T cells. However, this difference was not significant (0.1576 ± 0.0025 versus 0.1896 ± 0.0121, $P = 0.91$; Fig. 2*A*). The cell viability of the tumor cells cultured alone was significantly greater compared to the viability of the tumor cells cocultured with either the unlabeled or labeled B7-H3 CAR T cells (0.6803 ± 0.0306 versus 0.1896 ± 0.0121 or 0.1576 ± 0.0025, $P < 0.0001$).

The release of interferon-gamma (IFN-γ) by the stimulated anti-B7-H3 CAR T cells was maintained following mechanoporation. The concentration of IFN-γ was significantly greater in the labeled and unlabeled anti-B7-H3 CAR T cells coincubated with MG63.3 cells compared to the NT T cells cocultured with the tumor cells (labeled B7-H3 CAR T cells: 32,476.28 ± 18,750.19 pg/mL and unlabeled B7-H3 CAR T cells: 33,637.16 ± 19,420.42 pg/mL versus NT labeled: 0.00 ± 0.00 pg/mL and NT unlabeled: 0.00 ± 0.00 pg/mL, $P < 0.0001$) (Fig. 2*B*). Moreover, cytokine release was not significantly different in unlabeled and labeled T cells alone (1127.21 ± 650.79 pg/mL versus 0.00 ± 0.00 pg/mL, $P > 0.99$) nor for unlabeled and labeled activated T cells coincubated with the tumor cells (33,637.16 ± 19,420.42 pg/mL versus 32,476.28 ± 18,750.19 pg/mL, $P > 0.99$). The concentration of IFN-γ was negligible in MG63.3 cells, unlabeled or labeled NT T cells cocultured with tumor cells. However, the concentration of IFN-γ in unlabeled and labeled activated T cells cocultured with tumor cells was significantly greater compared to the MG63.3 cells incubated alone (labeled B7-H3 CAR T cells: 32,476.28 ± 18,750.19 pg/mL and unlabeled B7-H3 CAR T cells: 33,637.16 ± 19,420.42 pg/mL versus MG63.3 only: 0.00 ± 0.00 pg/mL, $P < 0.0001$).

Detection limit of iron-labeled CAR T cells. Pellets of increasing numbers of ferumoxytol-loaded anti-B7-H3 CAR T cells underwent MRI and MPI to determine the minimum number of cells that could be detected with these imaging techniques. MRI of $2 \times 10^6 - 2 \times 10^4$ ferumoxytol-loaded B7-H3 CAR T cells demonstrated a significant shortening of the T2* relaxation time compared to the unlabeled cells ($2 \times 10^6 - 2 \times 10^4$; $P < 0.0001$

and 2×10^3; $P = 0.003$) and Ficoll-only samples ($2 \times 10^6 - 2 \times 10^4$; $P < 0.0001$; Fig. 2*C*). However, from the representative MR images, the pellets containing 2×10^4 T cells labeled with ferumoxytol were more clearly distinguishable from the unlabeled and Ficoll-only pellets when compared to the pellets containing 2×10^3 ferumoxytol-loaded cells. The MPI signal of 2×10^3 ferumoxytol-loaded B7-H3 CAR T cells was significantly different compared to controls ($P = 0.002$; Fig. 2*D*). Therefore, the detection limit was 2×10^4 ferumoxytol-loaded B7-H3 CAR T cells for MRI and 2×10^3 ferumoxytol-loaded B7-H3 CAR T cells for MPI.

Multimodal imaging of the ferumoxytol-labeled CAR T cells. The design of the osteosarcoma mouse model to evaluate the *in vivo* tumor accumulation of ferumoxytol-labeled CAR T cells with MRI, PAT, and MPI is summarized in *SI Appendix*, Fig. 3. We injected osteosarcoma-bearing mice intravenously with ferumoxytol-labeled B7-H3 CAR T cells (tumor + CAR + iron group), unlabeled B7-H3 CAR T cells (tumor + CAR group), or NT ferumoxytol-labeled T cells (tumor + NT + iron group). Control animals without tumors were injected with ferumoxytol-labeled B7-H3 CAR T cells (CAR + iron). Images were acquired prior to the injection of the T cells at Day 1 and at Weeks 1, 2, and 3 post infusion of the T cells (*SI Appendix*, Fig. 3).

On Day 1, the tumor demonstrated iron enhancement on the T2*-weighted MRI following intravenous injection of ferumoxytol-labeled B7-H3 CAR T cells and ferumoxytol-labeled NT T cells (Fig. 3*A*). At Week 1, the level of iron enhancement in the tumor increased only in the ferumoxytol-labeled B7-H3 CAR T-cell group. The iron signal in the tumor vasculature slowly dissipated, resulting in an increase in T2*-enhancement, perhaps indicating enhanced infiltration of the T cells in the tumor tissue and effective dilution of the iron level in the CAR T cells. At Weeks 2 and 4, the tumor signal returned to baseline values. By comparison, the iron signal in the tumor disappeared at Week 1 after treatment with the ferumoxytol-labeled NT T cells, suggesting a lack of tumor infiltration and expansion of the non–tumor-targeted T cells. Animals injected with unlabeled B7-H3 CAR T cells did not show any tumor enhancement (Fig. 3*A*), demonstrating the necessity of ferumoxytol-loading for *in vivo* cell-tracking.

Accordingly, quantitative analysis revealed significant shortening of the tumor T2* relaxation time after the infusion of the ferumoxytol-labeled B7-H3 CAR T cells at Day 1 (10.88 ± 0.82 ms, $P = 0.04$) and Week 1 (9.11 ± 0.82 ms, $P < 0.0001$) compared to pretreatment images (13.85 ± 0.41 ms). At later time points (W2 and W3), the tumor T2* relaxation times (W2: 12.12 ± 0.52 ms and W3: 11.94 ± 0.25 ms) were not significantly different compared to the precontrast scans ($P > 0.999$). Following the injection of ferumoxytol-labeled NT T cells, a minor shortening of the T2* relaxation time was noted at Day 1, but it was not significantly lower when compared to the pretreatment images (11.94 ± 0.31 ms versus 13.96 ± 0.79 ms, $P = 0.68$). Following the injection of the unlabeled B7-H3 CAR T cells, the T2* values in osteosarcomas were not significantly different compared to the pretreatment values at any time point of observation (D1: 13.77 ± 0.37 ms, $P > 0.99$; W1: 13.91 ± 0.37 ms, $P > 0.99$; W2: 12.05 ± 0.18 ms, $P = 0.39$; and W3: 12.35 ± 0.40 ms, $P = 0.62$ versus Pre: 14.58 ± 0.54 ms; Fig. 3*B*).

Accumulation of ferumoxytol-labeled CAR T cells in osteosarcomas, as determined with MRI at Week 1, correlates with a decrease in tumor size at Week 3. The tumor size was not significantly different in the four experimental groups prior to treatment (Fig. 3*C*; $P > 0.99$). Following the infusion of the ferumoxytol-labeled B7-H3 CAR T cells, an initial increase in tumor size was noted during the first week when compared to the tumor size at baseline (D1: 42.91 ± 1.91 mm^2 and W1: 45.39 ± 0.41 mm^2 versus Pre: 37.24 ± 1.08 mm^2). Next, a decrease in the tumor size at Week 2 (35.15 ± 1.20 mm^2) and a 13-fold decrease in the tumor size at Week 3 (2.86 ± 1.13 mm^2, $P < 0.0001$) was observed when compared to the pretreatment images. A comparison of the tumor size in the animals treated with ferumoxytol-labeled and unlabeled B7-H3 CAR T cells showed that the tumor size was not significantly different at any time point of observation ($P > 0.99$) in both groups, indicating that labeling with ferumoxytol did not affect the ability of the B7-H3 CAR T cells to eradicate tumor cells *in vivo*. By comparison, the size of the tumors in the animals treated with ferumoxytol-labeled NT T cells significantly increased over time on W1 (72.99 ± 2.70 mm^2), W2 (89.05 ± 5.13 mm^2), and W3 (105.64 ± 4.11 mm^2) when compared with the pretreatment value (42.90 ± 0.48 mm^2, $P < 0.0001$). Moreover, caliper measurements were consistent with the tumor-size measurements based on the MR-imaging (*SI Appendix*, Fig. 4).

To evaluate whether MRI could predict tumor response to therapy, we correlated tumor T2* values at W1 with the tumor size measurements at W3. For animals treated with ferumoxytol-labeled B7-H3 CAR T cells, we found a significant correlation ($r = 0.45$, $P < 0.001$) between tumor T2* values at W1 and the tumor-size measurements at W3. Therefore, our data suggest that ferumoxytol MRI could serve as a predictive biomarker for tumor response to B7-H3 CAR T-cell therapy.

Histology verifies the accumulation of the ferumoxytol-labeled CAR T cells at the tumor site. Histological analysis further supported the findings from the MRI, PAT, and MPI images. Osteosarcomas treated with the unlabeled and ferumoxytol-labeled anti-B7-H3 CAR T cells revealed widespread infiltration of CD3$^+$ T cells and Perl's Prussian blue staining exposed the colocalization of the CAR T cells labeled with iron at the tumor site in the group injected with ferumoxytol-labeled B7-H3 CAR T cells. By comparison, osteosarcomas treated with ferumoxytol-labeled NT T cells demonstrated sparsely distributed CD3$^+$ T cells and negative Prussian blue stains (*SI Appendix*, Fig. 5).

Ferumoxytol-enhanced MRI detects the accumulation of the iron-labeled CAR T cells in the tumor and off-target sites in a dose-dependent manner. To reinforce that ferumoxytol-enhanced MRI can be used to quantify the distribution of the iron-labeled CAR T cells, we evaluated the ability to visualize two doses of ferumoxytol-labeled CAR T cells using MRI. At 1 h post injection, BLI verified the biodistribution of viable anti-B7-H3 CAR T cells. The whole-body photon radiance was significantly greater in the animals treated with 2×10^7 T cells compared to animals injected with 1×10^7 T cells ($4.15 \times 10^7 \pm 3.78 \times 10^6$ p/sec/cm^2/sr versus $1.18 \times 10^7 \pm 7.32 \times 10^6$ p/sec/cm^2/sr, $P = 0.02$; Fig. 3*D* and *SI Appendix*, Fig. 6). On Day 1 after infusion of 2×10^7 or 1×10^7 iron-labeled B7-H3 CAR-nLuc T cells, spleens, livers, and tumors of experimental mice demonstrated strong negative (dark) iron enhancement on MRI (Fig. 3*D*). There was a cell concentration–dependent signal decline in the spleen, liver, and tumor at Day 1 and 3 compared to the pretreatment images. Initially on Day I, the MR signal of the spleens was significantly lower after injection of 2×10^7 compared to 1×10^7 ferumoxytol-labeled B7-H3 CAR-nLuc T cells (2.66 ± 0.39 versus 5.84 ± 0.77, $P = 0.04$), indicating enhanced accumulation of the iron-labeled B7-H3 CAR-nLuc T cells. Additionally, the MRI signal of the spleens was significantly lower after injection of iron-labeled B7-H3 CAR-nLuc T cells compared to controls (2×10^7: 2.66 ± 0.39, $P = 0.001$; 1×10^6: 5.84 ± 0.77, $P = 0.0003$ versus 9.04 ± 0.35). On Day 3, the spleens demonstrated a persistent negative MRI enhancement which was stronger after infusion of 2×10^7 T cells compared to 1×10^7 T cells (4.56 ± 0.72 versus 8.34 ± 0.29, $P = 0.02$) and compared to the unlabeled B7-H3 CAR-nLuc T cells (4.56 ± 0.72 versus 9.47 ± 1.03, $P = 0.003$; Fig. 3*E*).

Similarly, there was a significant dose-dependent MRI signal decline in the liver on Day 1 after infusion of 2×10^7 iron-labeled B7-H3 CAR-nLuc T cells compared to 1×10^7 iron-

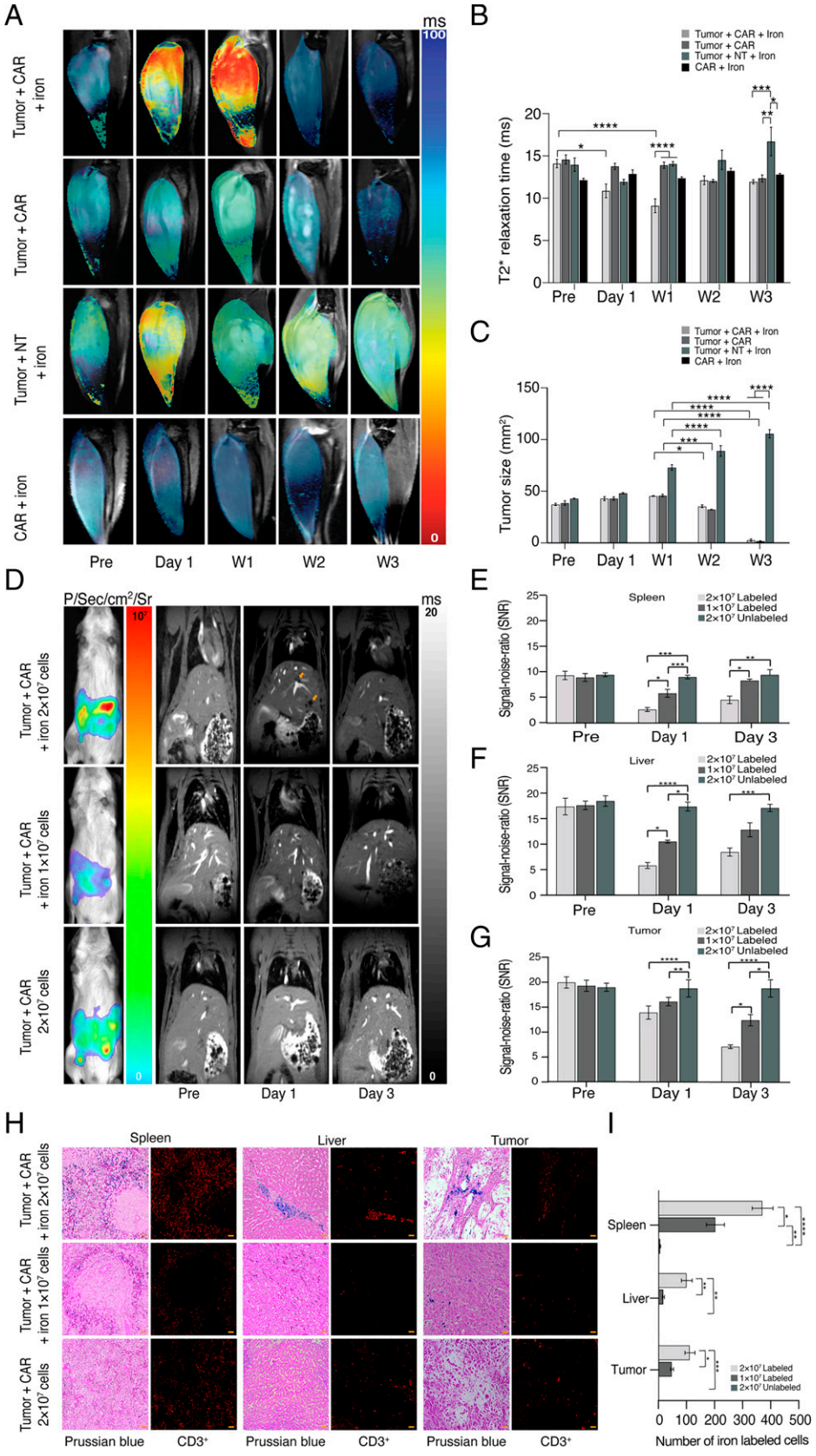

Fig. 3. Detection of ferumoxytol-labeled CAR T cells using MRI. (*A*) Representative coronal T2*-weighted MR images of the osteosarcomas in the tibia of experimental mice fused with superimposed, color-coded T2* maps. (*B*) Corresponding quantitative tumor T2* relaxation times at different time points before and after infusion of the anti-B7-H3 CAR T cells. There was significant enhancement of the tumor on Day 1 ($P = 0.04$) and Week 1 (W1, $P < 0.0001$) in the labeled tumor + CAR + iron group compared to the pretreatment images. (*C*) Serial tumor-size (millimeters^2) measurements on the MRI images noted a decrease in tumor size at W2 and W3 ($P < 0.0001$) in the labeled tumor + CAR + iron group. (*D*) Representative bioluminescence images acquired 1 h post injection confirmed the viability of the anti-B7-H3 CAR-nLuc T cells and coronal gradient echo MR images of animals injected with either 2×10^7 or 1×10^7 B7-H3 CAR-nLuc T cells visualized the colocalization of the iron-labeled CAR T cells to off-target sites (orange arrows). (*E–G*) Quantitative analysis indicated significantly greater and dose-dependent accumulation of the ferumoxytol-labeled anti-B7-H3 CAR-nLuc T cells in the spleens and livers of the animals treated with 2×10^7 T cells compared to animals injected with 1×10^7 T cells on Day 1 (spleen, $P = 0.04$; liver, $P = 0.049$). Alternatively, there was a dose-dependent enhancement of the signal in the tumor in the animals administered with 2×10^7 T cells compared to the animals injected with 1×10^7 T cells on Day 3 ($P = 0.04$). (*H*) Representative histological images of paraffin-embedded tissue sections obtained from mice on D3 post treatment stained with Prussian blue DAP (*Left*) as well as the anti-CD3 primary antibody and cy-5-conjugated secondary antibody (*Right*). (Scale bars, 50 μm.) Magnification is ×20. (*I*) Quantitatively, the localization of the iron-labeled B7-H3 CAR-nLuc T cells in the spleen, liver, and tumor was significantly greater in the animals administered with 2×10^7 T cells compared to the animals injected with 1×10^7 T cells (spleen, $P = 0.011$; liver, $P = 0.00$; and tumor, $P = 0.020$). Tumor + CAR + iron group (n = 5); animals injected with ferumoxytol-labeled CAR T cells, tumor + CAR group (n = 5); animals injected with unlabeled CAR T cells, tumor + NT + iron group (n = 5); animals injected with NT ferumoxytol-labeled T cells and CAR + iron group (n = 3); and animals without tumors injected with ferumoxytol-labeled CAR T cells. Tumor + CAR + iron 2×10^7 group (n = 5); animals injected with 2×10^7 ferumoxytol-labeled B7-H3 CAR-nLuc T cells, Tumor + CAR + iron 1×10^7 group (n = 4); animals injected with 1×10^7 ferumoxytol-labeled B7-H3 CAR-nLuc T cells, Tumor + CAR 2×10^7 group (n = 3); and animals injected with 2×10^7 unlabeled B7-H3 CAR-nLuc T cells. D = day, W = week, and NT = nontransduced. Data represents mean ± SEM. Statistical comparisons were performed using the one-way ANOVA with the Tukey's honest significant difference test.

labeled B7-H3 CAR-nLuc T cells (5.18 ± 0.35 versus 10.51 ± 0.29, $P = 0.049$) and compared to unlabeled cells (2×10^7: 5.18 ± 0.35, $P < 0.0001$; 1×10^7: 10.51 ± 0.29, $P = 0.006$ versus 17.37 ± 0.87). On Day 3, the liver MRI signal was significantly lower after infusion of 2×10^7 iron-labeled T cells compared to unlabeled cells (8.45 ± 0.80 versus 17.09 ± 0.71 $P = 0.0002$; Fig. 3*F*).

The tumors demonstrated a significant MRI signal decline after infusion of 2×10^7 or 1×10^7 ferumoxytol-labeled B7-H3

CAR-nLuc T cells compared with the unlabeled B7-H3 CAR-nLuc T cells on Day 1 (2×10^7: 13.92 ± 1.32, $P < 0.0001$; 1×10^7: 16.12 ± 0.84, $P = 0.007$ versus 18.76 ± 1.73; *SI Appendix*, Fig. 7 and Fig. 3*G*) and Day 3 of treatment (2×10^7: 7.07 ± 0.39, $P < 0.0001$; 1×10^7: 12.39 ± 1.12, $P = 0.03$ versus 15.59 ± 0.93). Moreover, the tumor signal intensity at Day 3 after injection of 2×10^7 iron-labeled B7-H3 CAR-nLuc T cells was significantly lower compared with the animals injected with the 1×10^7 iron-labeled B7-H3 CAR-nLuc T cells (7.07 ± 0.39 versus 12.39 ± 0.12 $P = 0.04$).

Perl's Prussian blue staining confirmed the distribution of the iron-labeled B7-H3 CAR-nLuc T cells in the tumor and off-target sites. The colocalization of the ferumoxytol-labeled B7-H3 CAR-nLuc T cells in the spleen, liver, and tumor was further verified by histological analysis on Day 3 post treatment (Fig. 3*H*). A significant dose-dependent, enhanced accumulation of the iron-labeled B7-H3 CAR-nLuc T cells was evident in the spleens of the animals administered with 2×10^7 T cells compared to animals treated with 1×10^6 T cells (370.60 ± 37.20 versus 202.50 ± 32.19, $P = 0.01$). Additionally, a significantly greater number of the ferumoxytol-labeled B7-H3 CAR-nLuc T cells accumulated in the spleens of animals treated with 2×10^7 or 1×10^7 iron-labeled B7-H3 CAR-nLuc T cells compared to controls (2×10^7: 370.60 ± 37.20, $P < 0.0001$; 1×10^7: 202.50 ± 32.19, $P = 0.01$ versus 5.67 ± 1.45). Similarly, a significantly greater number of the iron-labeled B7-H3 CAR-nLuc T cells colocalized in the livers of animals treated with 2×10^7 T cells compared to the animals administered with 1×10^7 T cells (100.60 ± 18.85 versus 17.25 ± 3.71, $P = 0.005$) and compared to animals administered with the unlabeled B7-H3 CAR-nLuc T cells (100.60 ± 18.85 versus 0.00 ± 0.00, $P = 0.002$). In addition, there was a significantly greater number of the ferumoxytol-labeled B7-H3 CAR-nLuc T cells in the tumors of animals administered with 2×10^7 T cells compared to animals treated with 1×10^7 T cells (111.80 ± 17.62 versus 48.00 ± 5.48, $P = 0.02$) and animals treated with unlabeled B7-H3 CAR-nLuc T cells (111.80 ± 17.62 versus 0.00 ± 0.00, $P = 0.001$; Fig. 3*I*).

Imaging of ferumoxytol-labeled CAR T cells with PAT. To confirm the MR-imaging findings, we also assessed whether the accumulation of ferumoxytol-labeled CAR T cells in the osteosarcomas can be visualized using PAT, a relatively inexpensive, clinically applicable modality that does not require the use of ionizing radiation. Following the intravenous injection of the ferumoxytol-labeled B7-H3 CAR T cells, a significant increase in the photoacoustic signal was evident at Week 1 compared to the pretreatment scans (15.87 ± 5.91% versus 4.66 ± 1.12%, $P = 0.04$; Fig. 4*A*). Similar to the signal kinetics observed on MRI, the photoacoustic signal was 2.3-fold lower in the second week compared to the first week (6.91 ± 2.67% versus 15.87 ± 5.91%; Fig. 4*B*) in the animals treated with the ferumoxytol-labeled B7-H3 CAR T cells. On Week 1, the photoacoustic signal of the tumors treated with ferumoxytol-labeled NT CAR T cells was significantly lower compared to the tumors treated with the ferumoxytol-labeled B7-H3 CAR T cells (3.95 ± 1.44% versus 15.87 ± 5.91%, $P = 0.03$). The photoacoustic signal did not significantly change in the animals treated with the unlabeled B7-H3 CAR T cells on W1 and W2 post infusion when compared to the pretreatment images (W1: 1.37 ± 0.65%, $P = 0.98$; W2: 5.01 ± 1.04%, $P > 0.99$ versus Pre: 4.97 ± 1.43%).

Analysis of the tumor volume using ultrasound indicated a significant increase in the tumor volume in the animals treated with the anti-B7-H3 CAR T cells labeled with ferumoxytol (Pre: 269.28 ± 12.96 mm^3; W1: 466.77 ± 10.59 mm^3, $P < 0.001$), unlabeled anti-B7-H3 CAR T cells (Pre: 294.83 ± 9.58 mm^3; W1: 412.52 ± 30.16 mm^3, $P = 0.04$), and NT T cells labeled with ferumoxytol (Pre: 266.03 ± 21.85 mm^3; W1: 452.08 ± 48.78 mm^3, $P < 0.001$) on Week 1 following infusion (Fig. 4 *C–E*). By the second week, the tumor volume in the animals injected with anti-B7-H3 CAR T cells labeled with ferumoxytol and unlabeled anti-B7-H3 CAR T cells was significantly lower than in the group injected with NT T cells labeled with ferumoxytol (313.14 ± 25.79 mm^3 and 228.51 ± 16.54 mm^3 versus 687.34 ± 12.55 mm^3, $P < 0.0001$). Additionally, the tumor volume in the animals administered with the anti-B7-H3 CAR T cells labeled with ferumoxytol and unlabeled B7-H3 CAR T cells was not significantly different on pre ($P > 0.99$), W1 ($P = 0.85$), and W2 ($P = 0.54$) images. Measurements of the oxygen saturation (SO_2) are described in the *SI Appendix*, Fig. 8.

Imaging of the ferumoxytol-labeled CAR T cells with MPI. While MRI is immediately clinically applicable, quantification of nanoparticle-induced MRI signal effects is complicated. MPI has the advantage that it allows for direct quantification of iron particles. In addition, MPI only displays the signal from the iron oxide nanoparticles without any background noise. MPI images after the intravenous infusion of the ferumoxytol-labeled B7-H3 CAR T cells confirmed the accumulation of anti-B7-H3 CAR T cells in the tumor tissue (Fig. 4*F*). Quantitatively, at Week 1, a significantly greater concentration of iron was detected in the tumors treated with the ferumoxytol-labeled B7-H3 CAR T cells compared to the animals infused with the unlabeled B7-H3 CAR T cells (5.56 ± 0.38 μg versus 0.21 ± 0.01 μg, $P < 0.0001$; Fig. 4*G*).

Following the infusion of the ferumoxytol-labeled NT CAR T cells, a significantly higher iron nanoparticle signal was noted at Week 1 compared to the animals injected with the unlabeled B7-H3 CAR T cells (2.86 ± 0.24 μg versus 0.21 ± 0.01 μg, $P < 0.0001$). However, this initial signal enhancement in the animals infused with the ferumoxytol-labeled NT CAR T cells was significantly lower compared to tumors treated with ferumoxytol-labeled B7-H3 CAR T cells during Week 1 (2.86 ± 0.24 μg versus 5.56 ± 0.38 μg, $P < 0.0001$) and Week 2 (0.18 ± 0.01 μg versus 3.87 ± 0.06 μg, $P < 0.0001$). By comparison, no MPI signal enhancement and no significant increase in the level of the iron oxide nanoparticles was noted in the tumor after infusion of unlabeled B7-H3 CAR T cells (W1: 0.21 ± 0.01 μg versus W2: 0.20 ± 0.01 μg, $P > 0.99$; Fig. 4*G*).

Discussion

We found that ferumoxytol-labeled CAR T cells could be detected in osteosarcomas with MRI, PAT, and MPI. These results demonstrated the use of ferumoxytol-enhanced MRI to monitor the trafficking of the CAR T cells in on-target and off-target sites in a dose-dependent manner. Real-time *in vivo* imaging of therapeutic CAR T cells can enhance our understanding of the variables that influence the accumulation of CAR T cells in the tumor microenvironment (39). Quantitative MRI is a dynamic and noninvasive tool that enables longitudinal imaging of labeled therapeutic cells (40–42). Previous imaging studies of T cells labeled with iron have detected human gamma delta T cells labeled with ferumoxytol *in vitro* (43), human anti-EGFRvIII CAR T cells labeled with ultrasmall, superparamagnetic iron oxide nanoparticles (20), murine pmel-specific DsRed T cells labeled with ferucarbotran (21), rat T cells labeled with superparamagnetic, nano-sized iron oxide nanoparticles trafficking to the heart and lung 48 h *in vivo* (15) using MRI, and mouse $CD4^+$ T cells labeled with fluorescently conjugated iron oxide nanoparticles using confocal microscopy (44, 45). In comparison, our study provided a microfluidics-based mechanical method for labeling human CAR T cells with ferumoxytol, and we used a multimodal approach to image intravenously infused CAR T cells labeled with iron *in vivo* in a preclinical model that has the potential for clinical translation. The feasibility for translation is demonstrated by the first in human study imaging CAR T cells labeled with copper-64 superparamagnetic iron oxide nanoparticles with dual PET-

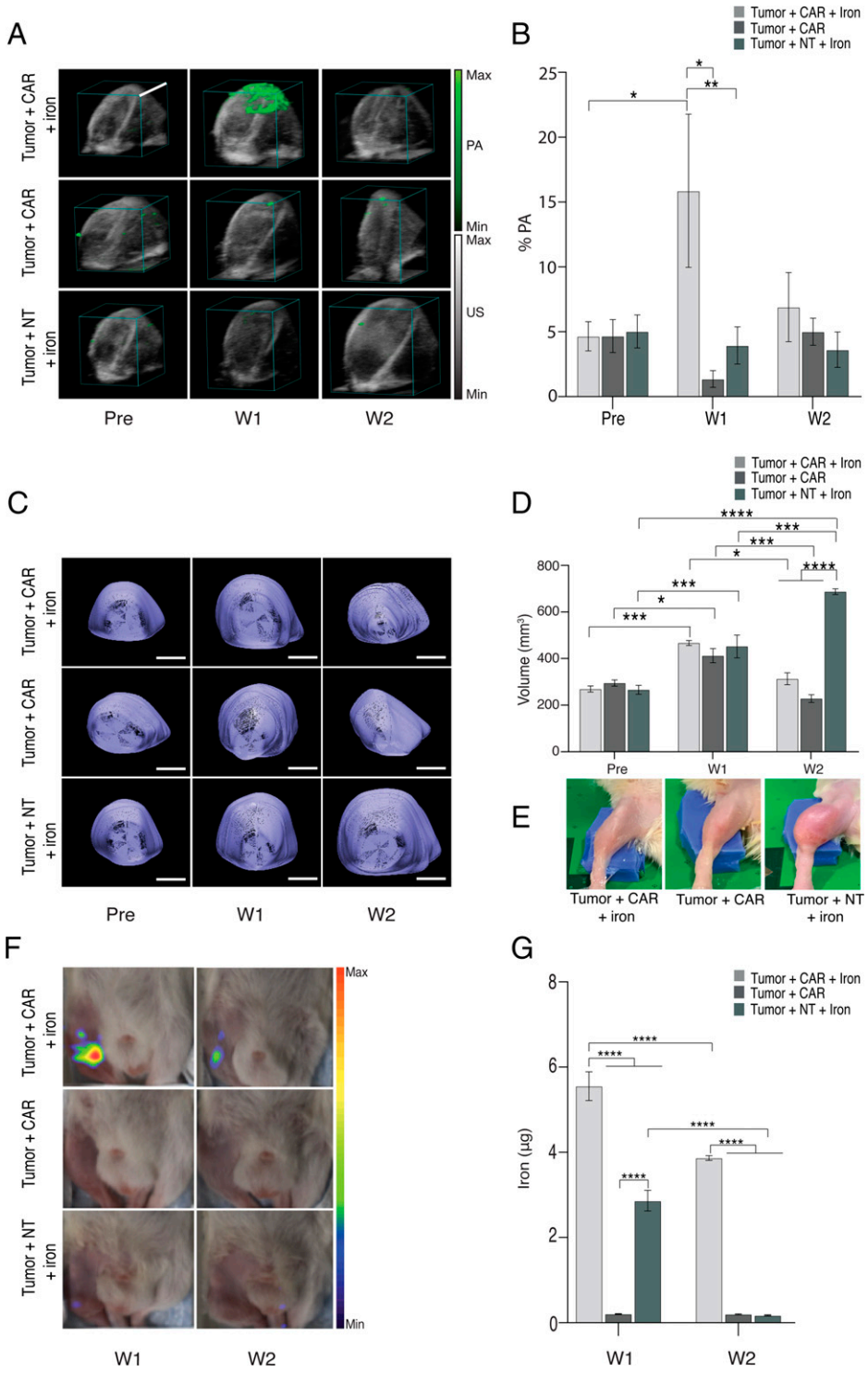

Fig. 4. Visualization of CAR T cells labeled with ferumoxytol using PAT and MPI. (*A*) Representative photoacoustic images showing the accumulation of CAR T cells labeled with ferumoxytol in the tumor + CAR + iron group (green). (Scale bar, 10 mm.) (*B*) Quantitative photoacoustic data demonstrating the percentage photoacoustic signal (% PA). (*C*) Representative 3D rendering of the photoacoustic images of osteosarcomas at different time points before and after CAR T-cell treatment. (Scale bars, 4 mm.) (*D*) Tumor volume (millimeters^3) was acquired by drawing ROI on the 3D-rendered photoacoustic images of osteosarcomas. At W2, there was a significant decrease in the tumor volume in both the tumor + CAR + iron ($P < 0.05$) and tumor + CAR ($P < 0.001$) groups when compared to the tumor + NT + iron group. (*E*) Representative bright-field images acquired on W2 postinfusion of the T cells showing the tibiae of the animals from the tumor + CAR + iron, tumor + CAR and tumor + NT + iron groups. (*F*) Representative MPI showed the detection of iron in the animals administered with CAR T cells labeled with ferumoxytol. (*G*) Quantification of the MPI data indicated that the level of iron was significantly greater ($P < 0.0001$) in the labeled tumor + CAR + iron group than in the unlabeled tumor + CAR and the untreated tumor + NT + iron groups. Tumor + CAR + iron group (n = 5); animals injected with ferumoxytol-labeled CAR T cells, tumor + CAR group (n = 5); animals injected with unlabeled CAR T cells, tumor + NT + iron group (n = 5); and animals injected with NT ferumoxytol-labeled T cells. D = day, W = week, and NT = nontransduced. Data represents mean ± SEM. Statistical comparisons were performed using the one-way ANOVA with the Tukey's honest significant difference test.

MR, which found that the functionality of the iron-labeled T cells was maintained and the labeled T cells remained persistent for an extended period of time in subjects (46).

Mechanoporation to label CAR T cells with ferumoxytol was chosen for a variety of reasons. Firstly, our specialized microfluidics device provided highly efficient labeling of more than 1 pg iron per cell (47). Others have achieved comparable labeling efficiencies following the incubation of pmel-specific DsRed T cells (1 pg/cell) with ferucarbotran (200 μg Fe/mL) for 24 h (21). Additionally, protamine sulfate was used to deliver ferumoxides (1.5 pg/cell) in mesenchymal stem cells (37) and cross-linked iron oxide nanoparticle to ovalbumin specific murine $CD8^+$ T cells (0.7 pg/cell) (13). Physical methods including electroporation (48), magnetofection (43) scrape loading (49), cavitation induction (50), microinjection (51), nanoneedles (52), and fluid shear loading (53) have been used for the delivery of biological material in cells. However, low recovery rate accompanied by a substantial decrease in cell viability limits the widespread use of these methods in clinical trials, in which the large-scale production of viable therapeutic cells is required. Contrary to the methods listed above, the cell viability and functionality was not significantly affected by our approach using mechanoporation. Secondly, ferumoxytol is FDA approved and immediately available for use in humans as an "off label" contrast agent (54, 55). It is currently used for intravenous iron supplementation in pediatric patients with iron deficiency anemia (27, 56) to visualize suspected venous occlusion in patients with renal failure using three-dimensional (3D) ferumoxytol-enhanced cardiovascular magnetic resonance venography and imaging macrophages in the human cerebral aneurysm walls (57). The iron oxide nanoparticle has desirable features; it is coated with a low–molecular weight semisynthetic carboxymethyl-dextran coat (58), which is desirable for labeling T cells because it consists of hydroxyl and carboxyl functional groups that allow efficient chemical modification. The coating also exhibits high biocompatibility, biodegradability, and solubility in water (59). Thirdly, a transfection reagent is not required for the labeling of the T cells with ferumoxytol by mechanoporation. The use of the transfection agents for introducing macromolecules in T cells has been shown to have detrimental effects on immune cell function, and many agents are not clinically translatable. Transfection of human primary immune cells with polymer or lipid-based nanoparticles using lipofectamine 2000 resulted in a reduction in the expression of genes that are vital for immune cell proliferation (35), while lipofection of cytokine-induced killer lymphocytes led to the induction of apoptosis, characterized by the enhanced secretion of the tumor necrosis factor alpha (TNFα) in the transfected cells than in the control nontransfected cells (36).

Labeling of T cells with iron did not affect the viability and function of murine $CD8^+$ T cells (43), murine $CD4^+$ T cells (44), and rat T cells (15). In addition, following stimulation by lipopolysaccharide, Jurkat T cells labeled with polyethylene glycol–coated, superparamagnetic iron oxide nanoparticles, IOPC-NH_2 (0.57 ± 0.12 pg iron/T-cell) demonstrated similar levels of the release of interleukin-6 and TNF-α cytokines compared to unlabeled T cells (15). Conversely, we demonstrated that the cell viability of the anti-B7-H3 CAR T cells pre- and post labeling was maintained (Fig. 1*D*) and the proliferation of the ferumoxytol-labeled T cells from Day I to 5 was persistent (Fig. 1*E*). Additionally, the coculture assays confirmed that the ability of the ferumoxytol-labeled T cells to decrease the cell viability of the MG63.3 cells and the release of IFN-γ was sustained (Fig. 2 *A* and *B*). Furthermore, the ferumoxytol-labeled B7-H3 CAR T cells exhibited a comparable pattern of tumor remission in animals administered with the unlabeled and ferumoxytol-labeled B7-H3 CAR T cells (Fig. 3 *A–C* and Fig. 4 *C–E*), indicating that mechanoporation-labeling with ferumoxytol did not impair the function of the CAR T cells. Moreover, histology data illustrated the colocalization of iron-labeled anti-B7-H3 CAR T cells in the tumor site (Fig. 3 *H* and *I* and *SI Appendix*, Fig. 5). This further verified that the MRI, PAT, and MPI signals corresponded to the accumulation of the iron-labeled T cells at the tumor site. Overall, ferumoxytol-labeled anti-B7-H3 CAR T cells have maintained their ability to proliferate, decrease the viability of the MG63.3 cells, release IFN-γ, and migrate to the tumor site to exert antitumor effects that were evident by the decreased tumor sizes that were measured by multiple modalities.

Iron regulation plays a critical role in immunometabolism, particularly for T-cell development, activation, and proliferation (60, 61). We found that the PDT of the iron-labeled B7-H3 CAR T cells was 1.35-fold faster compared to the unlabeled B7-H3 CAR T cells (*SI Appendix*, Fig. 2). The exact mechanism in which exogenous iron enhances the proliferation of CAR T cells remains to be defined. Nevertheless, treatment of $CD4^+$ T cells with the iron chelator deferoxamine mesylate (DFO) to reduce the levels of endogenous iron resulted in the inhibition of T-cell proliferation in a dose-dependent manner, a sharp decrease in mitochondrial function, as well as a reduction in the surface expression of the transferrin receptor protein 1, ferritin, and ferroportin. Furthermore, insufficient iron levels led to defective 1L-2 receptor–mediated signaling in DFO-treated $CD4^+$ T cells, suggesting that iron modulated T-cell proliferation by intracellular IL-2-signaling (62).

We found significant MRI signal effects of ferumoxytol-labeled T cells. This is in accordance with a previous *in vitro* study in which imaging of ferucarbotran-labeled human cytomegalovirus–specific cytotoxic T lymphocytes revealed shortening of the T2*-relaxation times on day 0, 2, and a lack of detection after 14 d (63). Near-infrared dyes have frequently been used to detect T cells with PAT (64), and iron oxide nanoparticles have previously been used as contrast agents in PAT (65–67). However, studies on PAT imaging of T cells labeled with iron oxide nanoparticles are sparse. Similarly, MPI has not yet been widely used to monitor iron-labeled T cells, although recently, imaging of ferucarbotran-labeled, pmel-specific DsRed T cells in mice bearing KR158B glioblastomas at 24 h post intravenous injection was reported (21).

Limit of detection and defining the optimal-imaging window are essential considerations for clinical utilization of a molecular-imaging strategy. Our *in vitro* studies indicated the ability to visualize T-cell pellets containing 2×10^4 cells with MRI and T-cell pellets containing 2×10^3 cells with MPI. Others have labeled human gamma delta T cells with ferumoxytol using protamine sulfate combined with magnetofection and detected 9×10^5 labeled cells *in vitro* using a 3 Tesla MRI scanner (43). The difference in the detection capability may be due to a variety of factors including the differences in type of T cells, efficiency of the labeling method, and the gradient strength of the instrumentation used. We found that the optimal time point for visualizing the ferumoxytol-labeled B7-H3 CAR T cells was on Week 1 post treatment, at which the T2*-relaxation times were the lowest (Fig. 3*B*). Imaging of the biodistribution of the iron-labeled B7-H3 CAR T cells revealed a dose-dependent and greater enhancement of the T1-weighted MRI signal in the spleen and liver at Day 1 than Day 3, while accumulation of the iron-labeled B7-H3 CAR T cells in the tumor was minimal at Day 1 and significantly pronounced by Day 3 (Fig. 3 *D–I* and *SI Appendix*, Fig. 7). This aligns with previous work that demonstrated the enhanced colocalization of lymphocytes labeled with anionic maghemite nanoparticles (1.3 ± 0.1 pg of iron per cell) in the spleens with limited accumulation in ovalbumin-expressing tumors at 24 h post treatment, while greater accumulation in the tumor was detected at 48h and 72 h post treatment (68, 69). Additionally, we found a marginal increase in the tumor size after 24 h. This may be a result of pseudoprogression, which is a prominent feature in various immunotherapy studies resulting from increased accumulation of effector cells in the tumor microenvironment (70, 71).

A potential use of our imaging strategy is in cell-based clinical trials, in which a baseline MR image of the patient would be acquired, followed by the therapeutic cells undergoing a rapid mechanoporation based cell-labeling procedure with iron oxide nanoparticles, which is suitable for labeling therapeutic doses of cells within a relatively short amount of time without affecting the cell viability proliferation and function. Subsequently, the labeled cells would be administered in the patient, and follow-up MR-imaging would be performed at early time points and the shortening of the T2* or T1 relaxation times would be utilized as an imaging biomarker to quantify the localization of the therapeutic cells. While an osteosarcoma model is used here, it is possible to use this imaging strategy for tracking other therapeutic cells including CAR T cells targeted to glioblastoma, where strategies for tracking therapeutic cells in the brain are limited.

Conclusion

This work has demonstrated the feasibility of using a microfluidics platform to mechanically label CAR T cells with iron oxide nanoparticles with a labeling efficiency that is capable of detecting adoptively transferred T cells labeled with iron using MRI, PAT, and MPI. The imaging approach can be used to monitor the localization of the therapeutic cells in a dose-dependent manner and contribute to elucidating the factors that give rise to responders and nonresponders of T-cell therapy for solid tumors.

Methods

Generation of the Anti-B7-H3 CAR T Cells. All cell culture medium and supplements were obtained from Thermo Fisher Scientific unless otherwise stated. Additional methodological details are provided in *SI Appendix*. The retroviral vector used for the anti-B7-H3-4–1BBζ CARs (3) and the B7H3-BBz-SYFP-P2A-NLuc CAR (72) have been described previously. Briefly, six B7-H3 single-chain variable fragments (scFv) were codon optimized followed by synthesis by GeneArt (Life Technologies). Subsequently, they were introduced in a murine stem cell–based splice-gag vector (MSGV1) comprised of a CD8-α hinge-transmembrane domain, a CD137 (4-1BB) costimulatory motif, and a CD3ζ-signaling domain. A construct containing the CD3ζ-signaling domain and both 4–1BB and CD28 costimulatory motifs was used to test for the most efficient CARs. Moreover, a sequence of the human IgG1 constant domain (CH2 and CH3) was added between the transmembrane domain and the scFv. Customized Sequence verification (Macrogen) of the B7-H3 CAR constructs was performed (3). The B7-H3-4–1BBζ-BFP fusion protein was made using In-Fusion (Takara Bio, Mountain View) cloning techniques to add a BFP sequence downstream of the CD3ζ-signaling domain. For the B7H3-BBz-SYFP-P2A-NLuc CAR construct, the yellow fluorescent protein SYFP2 (73) was fused to the C terminus of the CD3ζ-signaling domain, using a P2A ribosome-skipping site (74) followed by NanoLuc luciferase (75). The production of the retroviral supernatant and the transduction of the isolated T cells was performed as previously described (76). The transduced CAR^+ T cells were detected by flow cytometry (BD Biosciences, San Jose), and the data were analyzed with the FlowJo software (Tree Star, Ashland).

T-Cell Labeling Using a Microfluidics Device. The design of the T-cell labeling microfluidics device was based on two previously developed devices that facilitated the sorting of viable cells and dead cells based on differences in their stiffness (38) and labeling of adipose-derived stem cells using ferumoxytol (47). The labeling device consisted of an inlet, outlet, and a central chamber made up of five channels containing multiple angular chevron ridges that are 3.6 μm to accommodate the labeling of the T cells with the ferumoxytol (Feraheme, AMAG Pharmaceuticals, Waltham) through a process known as cell volume exchange for convective transfer. The labeling chambers were molded in polydimethylsiloxane (PDMS) and plasma bonded using a PDC-32G Harrick (Harrick Plasma, Ithaca) to a glass slide. A standard two-step photolithography on a silicon wafer was used to generate an epoxy resin SU-8 mold. The microfluidic channel was formed by mixing a 10:1 ratio of PDMS and the crosslinking agent that was poured on the SU-8 mold. This was followed by degassing of the PDMS in a vacuum chamber and curing for 1 h at 80 °C. Once the PDMS had cooled, it was removed from the mold to allow for the indentation of the inlet and outlet using biopsy punches. Finally, the PDMS was bonded to clean glass slides, placed in a 80 °C oven for 1 h, and cooled. A solution of 1% bovine serum albumin (BSA, Sigma-Aldrich, St Louis) in 1× phosphate buffer saline (PBS) was left to flow through the chamber overnight at 4 °C (77). The B7-H3 CAR T cells (8×10^6/mL) were isolated from culture and resuspended in flow buffer containing 0.04% ethylenediaminetetraacetic acid and 0.1% BSA in 1× PBS. Ferumoxytol was added to the CAR T cells at a concentration (10 mg iron/mL) that has been previously reported to result in the uptake of 1 to 10 pg per cell, which aligns with the minimum level of iron required for detection with MRI (1 pg per cell) (78, 79). The hydrodynamic diameter of the FDA-approved ferumoxytol iron oxide particles is 20 to 30 nm with a Zeta potential of ×24.4 ± 9.32 mV. These iron oxide nanoparticles have an r1 relaxivity of 15 mM^{-1}/s^{-1} and a r2 relaxivity of 89 mM^{-1}/s^{-1} at 1.5 Tesla and 37 °C (80).

The CAR T cells and iron oxide nanoparticle suspension was infused through the inlet of the microfluidics device at a rate of 0.65 mL/min using a syringe pump (PHD 2000, Harvard Apparatus). Within the central microfluidics chamber, the cells permeate through multiple ridges where they are compressed, resulting in a transient loss of the intracellular volume. When the cell volume is recovered, connective fluid transfer occurs, resulting in the surrounding fluid containing the ferumoxytol nanoparticles accumulating in the cells. The lower that the size of the ridges is, the higher the compression rate and the volume loss, resulting in higher intracellular delivery of the iron oxide nanoparticles when the cell recovers (81). The labeled CAR T cells were collected from the outlet and washed twice using 1× PBS. Triplicate samples of the iron-labeled as well as unlabeled CAR T cells (2×10^5/mL) were prepared, and the cellular iron uptake was determined with ICP-OES (Optima 5300 DV, Perkin-Elmer, Waltham). Additionally, DAB-enhanced Perl's Prussian blue staining was performed on a subset of the unlabeled and labeled CAR T cells to detect the intracellular labeling of the CAR T cells with iron using the BZ-X700 series fluorescence microscope (Keyence, Itasca).

***In Vitro* Characterization of the Ferumoxytol-Labeled CAR T Cells.**

Detection with MRI and MPI. The limit of detection of the ferumoxytol-labeled CAR T cells with MPI and MRI was assessed by preparing a serial dilution of the labeled (2×10^3, 2×10^4, 2×10^5, 2×10^6), unlabeled CAR T cells (2×10^6), and a Ficoll-only solution. The samples containing T cells were pelleted and placed in either NMR glass tubes (Sigma-Aldrich, St. Louis) for MR-imaging using the 7T MR scanner (Bruker Biospin, Billerica) consisting of an eight-channel radiofrequency coil or 1-mL Eppendorf tubes for MPI using the Momentum MPI scanner (Magnetic Insight Inc, Alameda), which is a projection field-free line scanner operating with a magnetic field gradient strength of 6 × 6T/m. The imaging parameters for the *in vitro* MRI were a multi-echo spin echo sequence with a repetition time (TR) of 1,200 ms, echo time (TE) of 10, 20, 30, 40, 50, 60, 70, and 80 ms, flip angle (FA) of 90°, 192 × 192 matrix size, 1.1-mm slice thickness (SL), acquisition time (TA) of 13 min, 14-cm field of view (FOV), and a fast spin echo sequence with fat saturation (TR = 2,700 ms, TE = 32 ms, FA = 110° matrix size = 192 × 192, SL = 1 mm, FOV = 14 cm, and TA =16 min).

Viability and Proliferation. The viability and proliferation of the anti-B7-H3 CAR T cells was assessed before and immediately after passage through the microfluidics device using the trypan blue exclusion method and at Day 1, 3, and 5 post labeling using the colorimetric CCK-8 (Sigma-Aldrich, St. Louis). Cell counting using the CCK-8 is a stable method for assessing the cell number of viable cells in cytotoxicity and proliferation assays with a higher detection sensitivity than assays using other tetrazolium salts such as MTT, XTT, MTS, or WST-1. The CCK8 assay utilizes a tetrazolium salt that is reduced to an orange water-soluble formazan product by dehydrogenases in viable cells. The amount of formazan produced is directly proportional to the number of living cells, and it is detected by absorbance at 490 nm.

The anti-B7-H3 CAR T cells were coincubated with the MG63.3 cells to evaluate their viability and proliferation in the presence of the tumor antigen. Human MG63.3 osteosarcoma cells (1×10^6/mL) were plated on a tissue culture–treated round-bottom 96-well plate (Thermo Fisher Scientific, Hampton, NH). Following adhesion of the tumor cells, the medium was aspirated, and the labeled or unlabeled B7-H3 CAR T cells (1×10^6/mL) were added to the MG63.3 cells. The tumor and B7-H3 CAR T cells were cocultured while controls were incubated alone for 48 h. The CCK-8 assay was used to determine the proliferation of the MG63.3 osteosarcoma cells that were cocultured with the unlabeled or labeled CAR T cells, MG63.3 cells cultured alone, as well as the unlabeled and the labeled B7-H3 CAR T cells incubated alone.

Cytokine Release. A cytokine-release assay was used to evaluate the effect that mechanoporation-labeling had on the function of the B7-H3 CAR T cells. Human MG63.3 cells (1×10^6/mL) were plated and cocultured with either the labeled or unlabeled B7-H3 CAR T cells (1×10^6/mL) or incubated alone. The cocultures were coincubated for 24 h in medium that was not supplemented

with IL-2. The cells were subsequently spun down, the supernatant was harvested, and the concentration of IFN- γ was determined by enzyme-linked immunosorbent assay (R&D Systems, Minneapolis).

Multimodal *In Vivo* Imaging of CAR T Cells.

Mouse osteosarcoma model. All animal procedures were carried out in accordance with the institutional ethics regulations detailed in the Stanford Administrative Panel on Laboratory Animal Care protocol. All animals were treated as established by the National Research Council's Guide for the Care and Use of Laboratory Animals. All animal procedures were performed under isoflurane. Male nonobese diabetic scid gamma mice 8 wks-old (Jackson Laboratory, n = 30) were used. For the longitudinal *in vivo* model (n = 18), 15 animals were anesthetized and injected with human MG63.3 (1×10^6) cells into the right tibia, which led to intra- and extraosseous tumors similar to the tumors encountered in human patients. Three animals did not receive tumor injections. An additional 12 animals were injected with human MG63.3 (1×10^6) cells for the short-term *in vivo* model (n = 12). The tumor size was monitored weekly using a digital caliper, and the tumor area was calculated by multiplying the length of the major and minor axes. A total 4 wks following tumor inoculation, when the tumor size was 39.58 ± 1.0 mm^2, animals were intravenously injected with either 2×10^7 or 1×10^7 ferumoxytol-labeled B7-H3 CAR T cells, ferumoxytol-labeled NT T cells, or unlabeled B7-H3 CAR T cells. The three animals that were not administered with the tumor cells received 2×10^7 ferumoxytol-labeled B7-H3 CAR T cells. The administration of 1×10^7 or 2×10^7 CAR T cells is within the range of the dose used in a clinical setting, which typically range from 1×10^5/kg to 1×10^{10}/kg CAR T cells (82, 83). Longitudinal *in vivo* imaging was performed on the animals prior to the infusion of the B7-H3 CAR T cells and over a period of 3 wks post treatment and short-term imaging of the biodistribution of the B7-H3 CAR-nLuc T cells in on-target and off-target tissues was conducted over a 3-d period.

MRI Acquisition and Processing. Imaging using MRI was performed at 4 wks post tumor inoculation (preferumoxytol), 24 h after T-cell infusion, as well as 1, 2, and 3 wks following T-cell injection (post ferumoxytol). The pre ferumoxytol MRI was acquired to ensure that all osteosarcoma-bearing animals had tumors with an average size of 39.58 ± 1.0 mm^2, and the post ferumoxytol MRI was performed to monitor the trafficking and distribution of the ferumoxytol-labeled B7-H3 CAR T cells at the tumor and off-target sites. The following pulse sequences were used before and after intravenous injection of the T cells: T2 multi-echo gradient echo sequence with a TR of 2,400 ms, TE of 33 ms, and an FA α: 80°, a multi-echo spin echo sequence with a TR of 1,000 ms, TE of 3.07, 7.38, 11.70, 16.01, 20.33, 24.65, 28.96, 33.28, 37.59, and 41.91 ms, and α: 90°, and am FOV of 3 cm × 3 cm and an SL of 0.75 mm. A spoiled gradient recalled (SPGR) echo sequence was used for imaging the biodistribution of the iron-labeled CAR T cells in the spleen and liver. The SPGR sequence had a TR of 85.8 ms, TE of 1.8 ms α: 85°, a FOV of 4 cm × 4 cm, and an SL of 0.75 mm. The T2* relaxation times of the inner core and the whole tumor were generated by drawing regions of interest (ROIs) that were 14.08 ± 0.02 mm^2 on the generated T2* maps using the Osirix software version 8.0 (Pixmeo SARL, Bernex, Switzerland).

Photoacoustic and Ultrasound Imaging Acquisition and Processing. Prior to *in vivo* imaging, the photoacoustic properties of ferumoxytol and the iron-labeled anti-B7-H3 CAR T cells were assessed in an *in vitro* phantom study (*SI Appendix*, Fig. 9). For *in vivo* imaging, mice were anesthetized and fixed in the prone position. Photoacoustic and ultrasound images were collected using a Vevo 2100 LAZR imaging system (VevoLAZR, VisualSonics, Inc., Canada) with the photoacoustic-mode and ultrasound B-mode, respectively. Images rendered in 3D presented as a colored photoacoustic layer overlaid on top of the ultrasound images were produced using the VevoLAB software (VisualSonics, Inc., Canada). The "ROI" tool in VevoLAB was used to draw contours within the tibia and determine the volume of the ROI. For ferumoxytol images, the photoacoustic spectrum of ferumoxytol was imported, and the signal from ferumoxytol was isolated using the "multiplexing" tool. Multiplexed signals of oxygenated and deoxygenated hemoglobin were subtracted from the obtained ferumoxytol signal to reduce any interference caused by the background hemoglobin signal (67, 84). The photoacoustic signal produced from ferumoxytol was overlaid on the 3D-rendered ultrasound image and quantified as the percentage signal within the ROI.

MPI Acquisition and Processing. The post ferumoxytol images were obtained 1, 2, and 3, wks following T-cell infusion. The use of MPI to visualize iron oxide nanoparticles is emerging as a valuable molecular-imaging methodology due to its high resolution and sensitivity. An oscillating magnetic gradient is utilized to generate the MPI signal that increases linearly with increasing nanoparticle concentration and penetrates the tissue with negligible attenuation and zero background (85, 86). Samples are translated along the *z*-axis of the scanner using a single-axis translation stage, with field-free line along the *y*-axis and excitation field (45 kHz, 20-mT peak amplitude) along the *z*-axis. The x-space MPI reconstruction algorithm is used for image reconstruction (87–89). Two-dimensional coronal projection images of the animals were acquired (FOV, 6 cm × 10 cm), and to quantify the MPI signal, fiducials with known concentrations (0.03, 0.3, 3, and 30 mg/mL) of ferumoxytol were imaged. Image processing was performed using the VivoQuant software (InviCRO, Boston, MA) in which ROIs were drawn at the tumor site or fiducials and the signal linearity was measured using a linear-regression model. The MPI signal from the fiducials with known iron concentration was used to extrapolate the iron content at the tumor site (55).

Histology. On Day 3 post injection, the spleens, livers, and osteosarcoma xenografts were harvested, fixed in 4% paraformaldehyde in 1× PBS, embedded in paraffin, and cut using a microtome (Leica, Wetzlar, Germany) to produce sections that were 5 μm. Immunostaining of the paraffin-embedded sections was performed using an anti-CD3 antibody (1:150, AbCam, Cambridge) and the cy-5 AffiniPure Goat Anti-Rabbit IgG secondary antibody (1:1,000, Jackson Immuno Research Laboratories Inc., West Grove). Perl's Prussian blue staining to detect iron was performed by staining the fixed sections for 30 min in 2% potassium ferrocyanide and 2% hydrochloric acid and counterstaining with 0.5% eosin solution (Sigma-Aldrich, Oajville, Ontario, Canada) to identify the cytoplasm. A coverslip was placed on the dehydrated slides for imaging. Images were obtained using the BZ-X700 series fluorescence microscope (Keyence, Itasca).

Statistical Analysis. All *in vitro* labeling experiments were repeated at least three times, and an unpaired Student's t test was used to compare statistical significance between two experimental groups, while a one-way ANOVA with correction using the Tukey's honest significant difference post hoc test was used to assess the statistical significance between three or more groups. Data were visualized, and statistical analysis was performed using GraphPad Prism (version 6.0) as well as verified by a statistician. All data represents group mean values ± SEM. A $P < 0.05$ was considered statistically significant, and P values were denoted with asterisks as follows: $P > 0.05$; not significant, $^*P < 0.05$, $^{**}P < 0.01$, $^{***}P < 0.001$, and $^{****}P < 0.0001$.

Data Availability. All study data are included in the article and/or supporting information. All data have been deposited in the Open Science Framework, https://osf.io/4ysgn/?view_only=1cb265c8a49641828a399ab056df01b8.

ACKNOWLEDGMENTS. We acknowledge funding support from the Stanford University School of Medicine Department of Radiology. We thank Dr. Richard Barth in the Department of Radiology for providing seed funding for this project. This work was in part supported by a Technology Impact Award of the Cancer Research Institute and a Diversity Supplement award from the National Institute of Arthritis and Musculoskeletal and Skin Diseases (Grant 5R01AR054458-S). The imaging was performed at the Stanford Center for Innovation in *In vivo* Imaging (SCi^3). Small animal imaging for this project was supported by a shared resource of the Stanford Cancer Institute (P30CA124435). We thank M.E.M. for the shared MRI instrumentation grant (S10RR026917-01). We thank Dr. Laura Pisani in the Stanford Center for Innovation in *In Vivo* Imaging for assisting in the design of the MRI protocol. We thank Doreen Wu and Eric E. Peterson in the Stanford Animal Histology Services for assistance with the preparation of the histology specimens. We also thank Dr. Guangchao Li in the Environmental Measurements Facility for support with ICP-OES.

1. D. S. Geller, R. Gorlick, Osteosarcoma: A review of diagnosis, management, and treatment strategies. *Clin. Adv. Hematol. Oncol.* **8**, 705–718 (2010).
2. D. Ebb *et al.*, Phase II trial of trastuzumab in combination with cytotoxic chemotherapy for treatment of metastatic osteosarcoma with human epidermal growth factor receptor 2 overexpression: A report from the children's oncology group. *J. Clin. Oncol.* **30**, 2545–2551 (2012).
3. R. G. Majzner *et al.*, CAR T cells targeting B7-H3, a pan-cancer antigen, demonstrate potent preclinical activity against pediatric solid tumors and brain tumors. *Clin. Cancer Res.* **25**, 2560–2574 (2019).
4. J. R. Castellanos *et al.*, B7-H3 role in the immune landscape of cancer. *Am. J. Clin. Exp. Immunol.* **6**, 66–75 (2017).
5. R. A. Gardner *et al.*, Intent-to-treat leukemia remission by CD19 CAR T cells of defined formulation and dose in children and young adults. *Blood* **129**, 3322–3331 (2017).
6. D. W. Lee *et al.*, T cells expressing CD19 chimeric antigen receptors for acute lymphoblastic leukaemia in children and young adults: A phase 1 dose-escalation trial. *Lancet* **385**, 517–528 (2015).
7. M. Cazaux *et al.*, Single-cell imaging of CAR T cell activity in vivo reveals extensive functional and anatomical heterogeneity. *J. Exp. Med.* **216**, 1038–1049 (2019).

8. S. Srivastava, S. R. Riddell, Chimeric antigen receptor T cell therapy: Challenges to bench-to-bedside efficacy. *J. Immunol.* **200**, 459–468 (2018).
9. D. M. O'Rourke *et al.*, A single dose of peripherally infused EGFRvIII-directed CAR T cells mediates antigen loss and induces adaptive resistance in patients with recurrent glioblastoma. *Sci. Transl. Med.* **9**, eaaa0984 (2017).
10. F. C. Thistlethwaite *et al.*, The clinical efficacy of first-generation carcinoembryonic antigen (CEACAM5)-specific CAR T cells is limited by poor persistence and transient pre-conditioning-dependent respiratory toxicity. *Cancer Immunol. Immunother.* **66**, 1425–1436 (2017).
11. M. N. McCracken *et al.*, Noninvasive detection of tumor-infiltrating T cells by PET reporter imaging. *J. Clin. Invest.* **125**, 1815–1826 (2015).
12. N. Maximova, M. Gregori, F. Barbieri, A. Pizzol, A. Sonzogni, Safety and utility of percutaneous liver biopsy in hematopoietic stem cell transplant pediatric recipients: A retrospective study. *BMC Cancer* **16**, 590 (2016).
13. M. F. Kircher *et al.*, In vivo high resolution three-dimensional imaging of antigen-specific cytotoxic T-lymphocyte trafficking to tumors. *Cancer Res.* **63**, 6838–6846 (2003).
14. H. E. Daldrup-Link *et al.*, In vivo tracking of genetically engineered, anti-HER2/neu directed natural killer cells to HER2/neu positive mammary tumors with magnetic resonance imaging. *Eur. Radiol.* **15**, 4–13 (2005).
15. L. Liu *et al.*, Tracking T-cells in vivo with a new nano-sized MRI contrast agent. *Biol. Med. (Aligarh)* **8**, 1345–1354 (2012).
16. Y. Vedvyas *et al.*, Longitudinal PET imaging demonstrates biphasic CAR T cell responses in survivors. *JCI Insight* **1**, e90064 (2016).
17. K. V. Keu *et al.*, Reporter gene imaging of targeted T cell immunotherapy in recurrent glioma. *Sci. Transl. Med.* **9**, eaag2196 (2017).
18. M. A. Sellmyer *et al.*, Imaging CAR T cell trafficking with eDHFR as a PET reporter gene. *Mol. Ther.* **28**, 42–51 (2020).
19. F. Chapelin *et al.*, Fluorine-19 nuclear magnetic resonance of chimeric antigen receptor T cell biodistribution in murine cancer model. *Sci. Rep.* **7**, 1–12 (2017).
20. T. Xie *et al.*, Non-invasive monitoring of the kinetic infiltration and therapeutic efficacy of nanoparticle-labeled chimeric antigen receptor T cells in glioblastoma via 7.0-Tesla magnetic resonance imaging. *Cytotherapy* **23**, 211–222 (2021).
21. A. Rivera-Rodriguez *et al.*, Tracking adoptive T cell immunotherapy using magnetic particle imaging. *Nanotheranostics* **5**, 431–444 (2021).
22. J. A. Ronald *et al.*, A PET imaging strategy to visualize activated t cells in acute graft-versus-host disease elicited by allogenic hematopoietic cell transplant. *Cancer Res.* **77**, 2893–2902 (2017).
23. A. Badar *et al.*, Fluorescence-guided development of a tricistronic vector encoding bimodal optical and nuclear genetic reporters for in vivo cellular imaging. *Eur. J. Mol. Imaging* **5**, 18 (2015).
24. I. Minn *et al.*, Imaging CAR T cell therapy with PSMA-targeted positron emission tomography. *Sci. Adv.* **5**, eaaw5096 (2019).
25. S. S. Yaghoubi *et al.*, Noninvasive detection of therapeutic cytolytic T cells with 18F-FHBG PET in a patient with glioma. *Nat. Clin. Pract. Oncol.* **6**, 53–58 (2009).
26. S. R. Riddell *et al.*, T-cell mediated rejection of gene-modified HIV-specific cytotoxic T lymphocytes in HIV-infected patients. *Nat. Med.* **2**, 216–223 (1996).
27. M. Lu, M. H. Cohen, D. Rieves, R. Pazdur, FDA report: Ferumoxytol for intravenous iron therapy in adult patients with chronic kidney disease. *Am. J. Hematol.* **85**, 315–319 (2010).
28. A. M. Muehe *et al.*, Safety report of ferumoxytol for magnetic resonance imaging in children and young adults. *Invest. Radiol.* **51**, 221–227 (2016).
29. B. Zheng *et al.*, Quantitative magnetic particle imaging monitors the transplantation, biodistribution, and clearance of stem cells in vivo. *Theranostics* **6**, 291–301 (2016).
30. H. Nejadnik *et al.*, Ferumoxytol can be used for quantitative magnetic particle imaging of transplanted stem cells. *Mol. Imaging Biol.* **21**, 465–472 (2019).
31. S. Mohanty *et al.*, Nanoparticle enhanced MRI can monitor macrophage response to CD47 mAb immunotherapy in osteosarcoma. *Cell Death Dis.* **10**, 36 (2019).
32. D. M. Hasan *et al.*, Macrophage imaging within human cerebral aneurysms wall using ferumoxytol-enhanced MRI: A pilot study. *Arterioscler. Thromb. Vasc. Biol.* **32**, 1032–1038 (2012).
33. A. Khurana *et al.*, Ferumoxytol: A new, clinically applicable label for stem-cell tracking in arthritic joints with MRI. *Nanomedicine (Lond.)* **8**, 1969–1983 (2013).
34. H. Nejadnik *et al.*, The protein corona around nanoparticles facilitates stem cell labeling for clinical MR imaging. *Radiology* **286**, 938–947 (2018).
35. S. Przybylski *et al.*, Influence of nanoparticle-mediated transfection on proliferation of primary immune cells in vitro and in vivo. *PLoS One* **12**, e0176517 (2017).
36. O. Ebert *et al.*, Lymphocyte apoptosis: Induction by gene transfer techniques. *Gene Ther.* **4**, 296–302 (1997).
37. A. S. Arbab *et al.*, Efficient magnetic cell labeling with protamine sulfate complexed to ferumoxides for cellular MRI. *Blood* **104**, 1217–1223 (2004).
38. M. Islam *et al.*, Microfluidic sorting of cells by viability based on differences in cell stiffness. *Sci. Rep.* **7**, 1997 (2017).
39. C. H. June, M. Sadelain, Chimeric antigen receptor therapy. *N. Engl. J. Med.* **379**, 64–73 (2018).
40. C. M. Long, J. W. M. Bulte, In vivo tracking of cellular therapeutics using magnetic resonance imaging. *Expert Opin. Biol. Ther.* **9**, 293–306 (2009).
41. M. Srinivas, A. Heerschap, E. T. Ahrens, C. G. Figdor, I. J. M. de Vries, (19)F MRI for quantitative in vivo cell tracking. *Trends Biotechnol.* **28**, 363–370 (2010).
42. A. J. Theruvath *et al.*, Tracking stem cell implants in cartilage defects of minipigs by using ferumoxytol-enhanced MRI. *Radiology* **292**, 129–137 (2019).
43. G. M. Siegers, E. J. Ribot, A. Keating, P. J. Foster, Extensive expansion of primary human gamma delta T cells generates cytotoxic effector memory cells that can be labeled with Feraheme for cellular MRI. *Cancer Immunol. Immunother.* **62**, 571–583 (2013).
44. W. N. Jin *et al.*, Non-invasive tracking of CD4+ T cells with a paramagnetic and fluorescent nanoparticle in brain ischemia. *J. Cereb. Blood Flow Metab.* **36**, 1464–1476 (2016).
45. M. Kim *et al.*, Polyaspartamide-based graft copolymers encapsulating iron oxide nanoparticles for imaging and fluorescence labelling of immune cells. *Biomater. Sci.* **5**, 305–312 (2017).
46. R. Singla *et al.*, First in human study of in-vivo imaging of ex-vivo labelled CAR T cells with dual PET-MR. *Cytotherapy* **22**, S201 (2020).
47. H. Nejadnik *et al.*, Instant labeling of therapeutic cells for multimodality imaging. *Theranostics* **10**, 6024–6034 (2020).
48. M. Zhang *et al.*, The impact of Nucleofection® on the activation state of primary human CD4 T cells. *J. Immunol. Methods* **408**, 123–131 (2014).
49. M. Fechheimer *et al.*, Transfection of mammalian cells with plasmid DNA by scrape loading and sonication loading. *Proc. Natl. Acad. Sci. U.S.A.* **84**, 8463–8467 (1987).
50. P. Marmottant, S. Hilgenfeldt, Controlled vesicle deformation and lysis by single oscillating bubbles. *Nature* **423**, 153–156 (2003).
51. M. R. Capecchi, High efficiency transformation by direct microinjection of DNA into cultured mammalian cells. *Cell* **22**, 479–488 (1980).
52. D. Matsumoto *et al.*, Mechanoporation of living cells for delivery of macromolecules using nanoneedle array. *J. Biosci. Bioeng.* **122**, 748–752 (2016).
53. D. M. Hallow *et al.*, Shear-induced intracellular loading of cells with molecules by controlled microfluidics. *Biotechnol. Bioeng.* **99**, 846–854 (2008).
54. B. S. Spinowitz *et al.*, Ferumoxytol for treating iron deficiency anemia in CKD. *J. Am. Soc. Nephrol.* **19**, 1599–1605 (2008).
55. R. T. Castaneda, A. Khurana, R. Khan, H. E. Daldrup-Link, Labeling stem cells with ferumoxytol, an FDA-approved iron oxide nanoparticle. *J. Vis. Exp.* **4**, e3482 (2011).
56. I. C. Macdougall, W. E. Strauss, N. V. Dahl, K. Bernard, Z. Li, Ferumoxytol for iron deficiency anemia in patients undergoing hemodialysis. The FACT randomized controlled trial. *Clin. Nephrol.* **91**, 237–245 (2019).
57. D. M. Hasan *et al.*, Imaging aspirin effect on macrophages in the wall of human cerebral aneurysms using ferumoxytol-enhanced MRI: Preliminary results. *J. Neuroradiol.* **40**, 187–191 (2013).
58. J. P. Bullivant *et al.*, Materials characterization of Feraheme/ferumoxytol and preliminary evaluation of its potential for magnetic fluid hyperthermia. *Int. J. Mol. Sci.* **14**, 17501–17510 (2013).
59. J. M. Shin *et al.*, A carboxymethyl dextran-based polymeric conjugate as the antigen carrier for cancer immunotherapy. *Biomater. Res.* **22**, 21 (2018).
60. E. L. Pearce, Metabolism in T cell activation and differentiation. *Curr. Opin. Immunol.* **22**, 314–320 (2010).
61. S. J. F. Cronin, C. J. Woolf, G. Weiss, J. M. Penninger, The role of iron regulation in immunometabolism and immune-related disease. *Front. Mol. Biosci.* **6**, 116 (2019).
62. E. L. Yarosz *et al.*, Cutting edge: Activation-induced iron flux controls CD4 T cell proliferation by promoting proper IL-2R signaling and mitochondrial function. *J. Immunol.* **204**, 1708–1713 (2020).
63. A. J. Beer *et al.*, Visualization of antigen-specific human cytotoxic T lymphocytes labeled with superparamagnetic iron-oxide particles. *Eur. Radiol.* **18**, 1087–1095 (2008).
64. M. A. Kimm *et al.*, Longitudinal imaging of T cell-based immunotherapy with multispectral, multi-scale optoacoustic tomography. *Sci. Rep.* **10**, 1–12 (2020).
65. J. Reguera *et al.*, Janus plasmonic-magnetic gold-iron oxide nanoparticles as contrast agents for multimodal imaging. *Nanoscale* **9**, 9467–9480 (2017).
66. I. Monaco *et al.*, Synthesis of lipophilic core-shell Fe_3O_4@SiO_2@Au nanoparticles and polymeric entrapment into nanomicelles: A novel nanosystem for in vivo active targeting and magnetic resonance-photoacoustic dual imaging. *Bioconjug. Chem.* **28**, 1382–1390 (2017).
67. M. Gerling *et al.*, Real-time assessment of tissue hypoxia in vivo with combined photoacoustics and high-frequency ultrasound. *Theranostics* **4**, 604–613 (2014).
68. P. Smirnov *et al.*, In vivo cellular imaging of lymphocyte trafficking by MRI: A tumor model approach to cell-based anticancer therapy. *Magn. Reson. Med.* **56**, 498–508 (2006).
69. P. Smirnov *et al.*, In vivo single cell detection of tumor-infiltrating lymphocytes with a clinical 1.5 Tesla MRI system. *Magn. Reson. Med.* **60**, 1292–1297 (2008).
70. D. Brandsma, L. Stalpers, W. Taal, P. Sminia, M. J. van den Bent, Clinical features, mechanisms, and management of pseudoprogression in malignant gliomas. *Lancet Oncol.* **9**, 453–461 (2008).
71. L. C. Hygino da Cruz, Jr, I. Rodriguez, R. C. Domingues, E. L. Gasparetto, A. G. Sorensen, Pseudoprogression and pseudoresponse: imaging challenges in the assessment of posttreatment glioma. *AJNR Am. J. Neuroradiol.* **32**, 1978–1985 (2011).
72. J. Theruvath *et al.*, Locoregionally administered B7-H3-targeted CAR T cells for treatment of atypical teratoid/rhabdoid tumors. *Nat. Med.* **26**, 712–719 (2020).
73. G. J. Kremers, J. Goedhart, E. B. van Munster, T. W. Gadella, Jr; K. GJ, Cyan and yellow super fluorescent proteins with improved brightness, protein folding, and FRET Förster radius. *Biochemistry* **45**, 6570–6580 (2006).

74. J. H. Kim *et al.*, High cleavage efficiency of a 2A peptide derived from porcine teschovirus-1 in human cell lines, zebrafish and mice. *PLoS One* **6**, e18556 (2011).
75. M. P. Hall *et al.*, Engineered luciferase reporter from a deep sea shrimp utilizing a novel imidazopyrazinone substrate. *ACS Chem. Biol.* **7**, 1848–1857 (2012).
76. A. H. Long *et al.*, 4-1BB costimulation ameliorates T cell exhaustion induced by tonic signaling of chimeric antigen receptors. *Nat. Med.* **21**, 581–590 (2015).
77. A. Liu *et al.*, Microfluidic generation of transient cell volume exchange for convectively driven intracellular delivery of large macromolecules. *Mater Today (Kidlington)* **21**, 703–712 (2018).
78. S. Metz *et al.*, Capacity of human monocytes to phagocytose approved iron oxide MR contrast agents in vitro. *Eur. Radiol.* **14**, 1851–1858 (2004).
79. C. Heyn *et al.*, In vivo MRI of cancer cell fate at the single-cell level in a mouse model of breast cancer metastasis to the brain. *Magn. Reson. Med.* **56**, 1001–1010 (2006).
80. M. R. Bashir, L. Bhatti, D. Marin, R. C. Nelson, Emerging applications for ferumoxytol as a contrast agent in MRI. *J. Magn. Reson. Imaging* **41**, 884–898 (2015).
81. A. Liu *et al.*, Cell mechanical and physiological behavior in the regime of rapid mechanical compressions that lead to cell volume change. *Small* **16**, e1903857 (2020).
82. L. Zhao, Y. J. Cao, T. Engineered, Engineered T cell therapy for cancer in the clinic. *Front. Immunol.* **10**, 2250 (2019).
83. C. Zhang *et al.*, Phase I escalating-dose trial of CAR-T therapy targeting CEA^{+} metastatic colorectal cancers. *Mol. Ther.* **25**, 1248–1258 (2017).
84. L. J. Rich, M. Seshadri, Photoacoustic imaging of vascular hemodynamics: Validation with blood oxygenation level-dependent MR imaging. *Radiology* **275**, 110–118 (2015).
85. J. E. Lemaster, F. Chen, T. Kim, A. Hariri, J. V. Jokerst, Development of a trimodal contrast agent for acoustic and magnetic particle imaging of stem cells. *ACS Appl. Nano Mater.* **1**, 1321–1331 (2018).
86. G. Song *et al.*, Janus iron oxides @ semiconducting polymer nanoparticle tracer for cell tracking by magnetic particle imaging. *Nano Lett.* **18**, 182–189 (2018).
87. B. Gleich, J. Weizenecker, Tomographic imaging using the nonlinear response of magnetic particles. *Nature* **435**, 1214–1217 (2005).
88. R. M. Ferguson *et al.*, Magnetic particle imaging with tailored iron oxide nanoparticle tracers. *IEEE Trans. Med. Imaging* **34**, 1077–1084 (2015).
89. N. Panagiotopoulos *et al.*, Magnetic particle imaging: Current developments and future directions. *Int. J. Nanomedicine* **10**, 3097–3114 (2015).